

Spin-half paramagnetism in graphene induced by point defects

R. R. Nair et al.

#1 Quantitative analysis of fluorination of graphene laminates

Fluorination of graphene laminates was studied using different characterisation techniques such as Raman spectroscopy, X-ray photoelectron spectroscopy (XPS), and energy dispersive X-ray microanalysis (EDX). Raman spectroscopy provided a quick qualitative analysis of different levels of fluorination. This showed that the evolution of Raman spectra of graphene paper with fluorination (not shown) was very similar to the previously reported spectra for mechanically exfoliated single layer graphene [S1]. For quantitative determination of the fluorine-to-carbon ratio (F/C) after different fluorination times we employed XPS. Furthermore, the XPS results for several samples were corroborated by EDX.

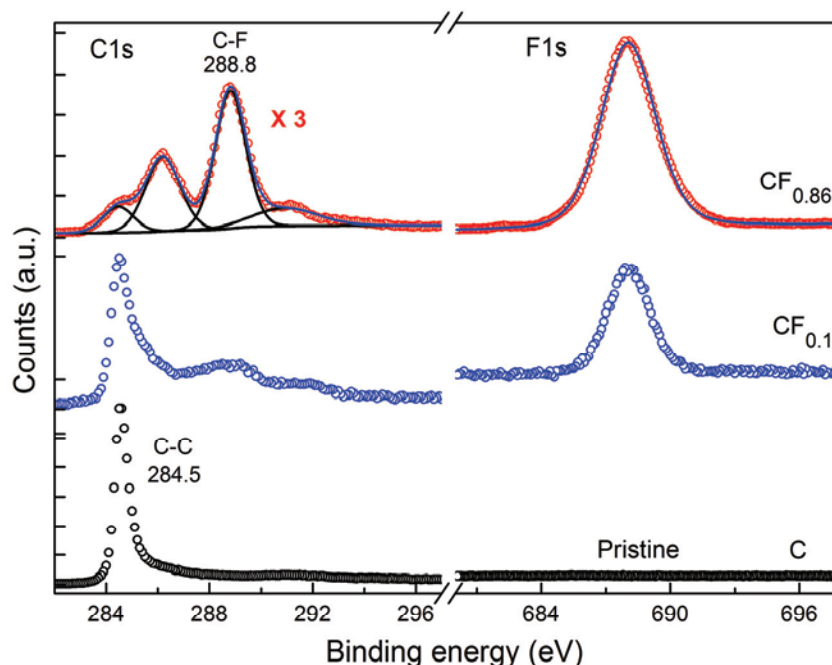


Figure S1. Typical examples of XPS spectra for pristine (bottom curve) and fluorinated (middle and top curves) graphene laminates at different degrees of fluorination.

XPS spectra were acquired on a Kratos Axis Ultra X-ray photoelectron spectrometer equipped with a monochromatic aluminium X-ray source and a delay line detector. Typical wide scan spectra were recorded from a 220 μm diameter area for binding energies between 0 and 1100 eV with a 0.8 eV step, at 160 eV pass energy. High resolution spectra of C1s and F1s peaks (such as those in Fig. S1) were recorded with a 0.1 eV step, at 40 eV pass energy.

Figure S1 shows typical XPS spectra for energies corresponding to C1s peaks of carbon (left part) and F1s peaks of fluorine (right part). The three C1s peaks indicate the presence of different types of carbon bonds while the strong F1s peak appearing after fluorination indicates the presence of chemisorbed fluorine. An intense peak at $\approx 284\text{ eV}$ in the spectrum of pristine graphene paper is due to the C-C sp^2 bonds in graphene [S1]. After exposure of graphene laminates to fluorine the intensity of this peak decreases while new peaks appear, corresponding to different types of C-F bonding. The intensities of these new peaks vary for different degrees of fluorination. The most pronounced peak at $\approx 289\text{ eV}$, in conjunction with the strong fluorine peak at $\approx 688\text{ eV}$, yield strong C-F covalent bonding [S2]. As Fig. S1 shows, the $\approx 688\text{ eV}$ peak is absent for pristine graphene laminates but shows strongly for all fluorinated samples, which again confirms the presence of covalently bonded fluorine. The other two peaks at $\approx 286.3\text{ eV}$ and 291 eV indicate the presence of C-CF and CF_2 bonds, respectively [S1, S3]. CF_2 and CF_3 bonds are expected to form primarily at defects or edges of graphene flakes. Note that the absence of CF_3 peaks ($\approx 293\text{ eV}$) and very small intensity of the CF_2 peaks indicates that fluorination in our samples occurs mainly at graphene surfaces, rather than at the defect sites or edges. As all graphene crystallites in the laminates are very small (typically 30-50 nm), bi- and trilayer graphene flakes (that are present in our laminates along with $\sim 50\%$ monolayers) are easily intercalated by F atoms.

The stoichiometric composition of different fluorinated samples was obtained by analysing the intensity of carbon and fluorine peaks using Casca XPS software [S4]. Spectra were taken from several $\approx 100\text{ }\mu\text{m}$ spots on each sample and the results averaged to obtain F/C for a particular fluorinated sample. This procedure indicated good spatial homogeneity of fluorination on a scale $\gg 100\text{ }\mu\text{m}$, as the calculated F/C ratios varied by no more than 5%. In addition, we carried out EDX analysis of several fluorinated samples, to confirm the stoichiometry, and found that the results were in full agreement with the XPS analysis above. These showed that for the longest fluorination time (80h) we were able to achieve $\text{F/C} \approx 1$, i.e. stoichiometric fluorographene. EDX analysis was also used to confirm that our fluorinated samples were free from contamination with metal impurities.

#2 Irradiation of graphene laminates with high-energy ions

For C^{4+} irradiations we used 5MV van de Graaf tandem accelerator where samples, mounted on aluminium foil, were clamped to a copper rod cooled with liquid nitrogen to $-50^{\circ}C$. The sample temperature, which was monitored using an infrared temperature sensor, remained below $50^{\circ}C$ during irradiation and the vacuum was maintained in the 10^{-6} - 10^{-7} mbar range. To ensure irradiation homogeneity, the focused beam spot was rasterized over the sample area using two perpendicular electromagnets. The fluence was determined from the total charge accumulated in the target chamber.

Proton irradiations were carried out in a 500kV ion implanter, at room temperature and energies between 350 and 400 keV and current densities $<0.2 \mu A/cm^2$. Two perpendicular electric fields were used to sweep the beam over the sample area and the radiation fluence was measured using four Faraday cups with a known window area. No considerable heating of the target is expected with the used energies and currents. The concentration of backscattered protons which stopped in the sample is estimated to be less than 1 ppm.

The fluences used to achieve the defect densities in Fig. 4 of the main text varied from $5 \cdot 10^{13}$ to $1 \cdot 10^{16} cm^{-2}$. We note that it was not possible to derive the defect density for each sample from the fluence alone, because different samples had different surface areas and different defect distributions. The defect densities shown in Fig. 4 (main text) were calculated for each sample on the basis of the corresponding fluence, surface area and the number of vacancies created by each type of ions as obtained from SRIM simulations.

To check for the possibility of vacancy-interstitial recombination during or after irradiation [S5], one of the proton-irradiated samples was annealed at $300^{\circ}C$ for 8h, which resulted in $\sim 20\%$ reduction in magnetic moment. This shows that the majority of vacancies in our samples do not recombine even at temperatures much higher than room temperature, in agreement with the higher mobility of interstitials in few-layer graphene compared to graphite [S6].

#3 Determination of the spin value from magnetisation data

To characterize the magnetic species contributing to the magnetization M of fluorinated and irradiated graphene laminates, we plotted M as a function of the reduced field H/T . For all samples (i.e. all degrees of fluorination and all vacancy concentrations) $\Delta M(H/T)$ curves measured at different temperatures collapse on a single curve, indicating that graphene with both types of defects behaves as a paramagnet with a single type of non-interacting spins. As an example, Fig.

S2(a) shows such analysis for the fully fluorinated graphene ($x=1$). The observed behavior is accurately described by the Brillouin function, such that the initial slope of $\Delta M(H/T)$ is determined by the angular momentum quantum number J and the g factor, and the saturation level is determined by the number of magnetic moments (spins) N :

$$M = NgJ\mu_B \left[\frac{2J+1}{2J} \text{ctnh} \left(\frac{(2J+1)x}{2J} \right) - \frac{1}{2J} \text{ctnh} \left(\frac{x}{2J} \right) \right]$$

where $x = gJ\mu_B H / k_B T$ and k_B the Boltzmann constant. Assuming $g=2$ (there are no indications in literature that g -factor in graphene may be enhanced), the Brillouin function provides excellent fits to the data for $J=S=1/2$ (red curve Fig. S2(a)). For comparison, we also show fitting curves for $J=1$, $3/2$ and 2 , all of which provide very poor fits, making it clear that only $J = S = 1/2$ fits the data.

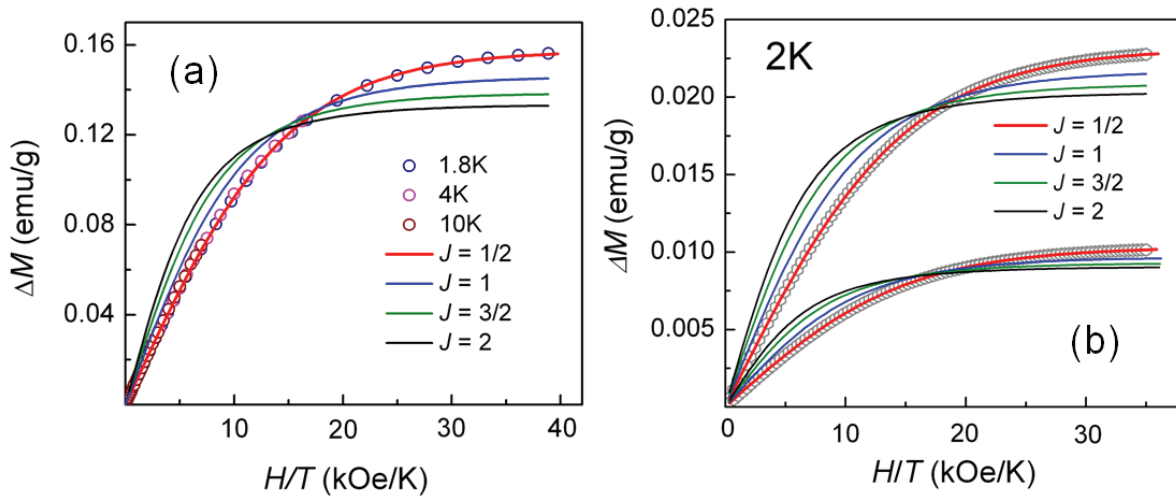


Figure S2. Determination of the angular momentum quantum number J from ΔM vs H/T curves. (a) Magnetisation of the fully fluorinated graphene crystallites, $x=1$ (linear diamagnetic background subtracted). Symbols are data for three different temperatures and solid curves are fits to the Brillouin function for $J=1/2$, 1 , $3/2$ and 2 . (b) Magnetisation due to vacancies: As the increase in M after irradiation was comparable to the paramagnetic signal in pristine graphene, ΔM here is the magnetisation over and above the paramagnetic contribution measured before irradiation (linear diamagnetic background subtracted as well). Grey symbols show data for two different vacancy concentrations (lower curve $2.4 \cdot 10^{19} \text{ g}^{-1}$, upper curve $7.4 \cdot 10^{19} \text{ g}^{-1}$) and solid lines show Brillouin function fits with $g=2$ and $J=1/2$, 1 , $3/2$ and 2 .

Figure S2(b) shows similar analysis for two different vacancy concentrations in graphene laminates irradiated with 350 keV protons. Again, only $J=S=1/2$ fits the data, with all other values of J giving very poor fits. This provides the most unequivocal proof that both types of point defects studied - fluorine adatoms and vacancies - represent non-interacting paramagnetic centers with spin $S=1/2$.

#4 Commentary on ferromagnetism reported for HOPG

Weak ferromagnetic signals ($\sim 10^{-3}$ emu/g) were found in pristine highly-oriented pyrolytic graphite (HOPG) (e.g. [S7,S8]) which, according to the authors, could *not* be explained by ~ 1 -2ppm of Fe detected using particle-induced X-ray emission (PIXE) or X-ray fluorescence spectroscopy (XRFS). Accordingly, the ferromagnetism was attributed to intrinsic defects, such as, e.g., grain boundaries [S8]. The ferromagnetic response was shown to increase dramatically after high-energy ion irradiation of HOPG [S9-S13], nanodiamonds [S14], carbon nanofoams [S15] and carbon films [S16]. Several scenarios have been suggested to explain the observed ferromagnetism.

Trying to clarify the situation, we have carried out extensive studies of magnetic behaviour of HOPG crystals obtained from different manufacturers (ZYA-, ZYB-, and ZYH-grade from NT-MDT and SPI-2 and SPI-3 from SPI Supplies). These crystals are commonly used for studies of magnetism in graphite; e.g., ZYA-grade crystals were used in refs. S7, S9-S13 and ZYH-grade in ref. S8. We have also observed weak ferromagnetism, similar in value to the one reported previously for pristine (non-irradiated) HOPG. Below, we show that the ferromagnetism in ZYA-, ZYB-, and ZYH-grade crystals is due to micron-sized magnetic inclusions (containing mostly Fe), which can easily be visualized by scanning electron microscopy (SEM) in the backscattering mode. Without the intentional use of this technique, the inclusions are easy to overlook. No such inclusions were found in SPI crystals and, accordingly, in our experiments these crystals were purely diamagnetic at all temperatures (no ferromagnetic signals at a level of 10^{-5} emu/g).

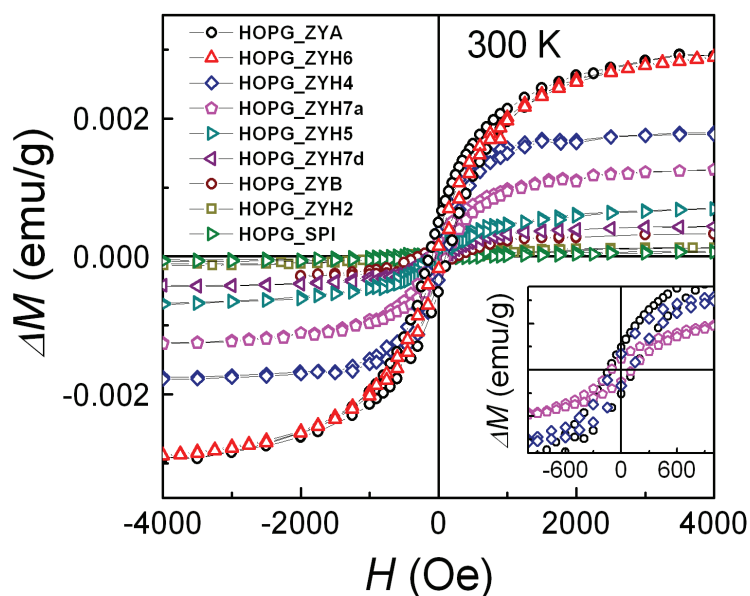


Figure S3. Ferromagnetic response in different HOPG crystals. Magnetic moment ΔM vs applied field H after subtraction of the linear diamagnetic background. The inset shows a low-field zoom of three curves from the main panel where the remnant ΔM and coercive force are seen clearly.

Ten HOPG crystals of different grades (ZYA, ZYB, ZYH and SPI) were studied using SQUID magnetometry (Quantum Design MPMS XL7), XRFS, SEM and chemical microanalysis by means of energy-dispersive X-ray spectroscopy (EDX). For all ZYA, ZYB and ZYH crystals, magnetic moment vs field curves, $M(H)$, showed characteristic ferromagnetic hysteresis in fields below 2000 Oe, which was temperature independent between 2K and room T , implying a Curie temperature significantly above 300K. The saturation magnetisation M_S varied from sample to sample by more than 10 times, from $1.2 \cdot 10^{-4}$ emu/g to $3 \cdot 10^{-3}$ emu/g – see Fig. S3. This is despite the fact that XRFS did not detect magnetic impurities in any of our HOPG crystals (with a detection limit better than a few ppm). This result is similar to the findings of other groups [e.g. S9, S10, S11, S16]. Figure S3 also shows an $M(H)$ curve for one of the SPI crystals, where no ferromagnetism could be detected.

The seemingly random values of ferromagnetic signal in nominally identical crystals could be an indication that the observed ferromagnetism is related to structural features of HOPG, such as grain boundaries, as suggested in ref. [S8]. However, we did not find any correlation between the size of the crystallites making up HOPG crystals and/or their misalignment and the observed M_S . For example, the largest M_S as well as the largest coercive force, M_C , were found for one of the ZYA crystals, which have the smallest mosaic spread (0.4 – 0.7°), and for a ZYH crystal with the largest mosaic spread (3 – 5°). Furthermore, crystallite sizes were rather similar for all ZYA, ZYB and ZYH crystals (see Fig. S4) while M_S varied by almost a factor of 3 (see Fig. S3).

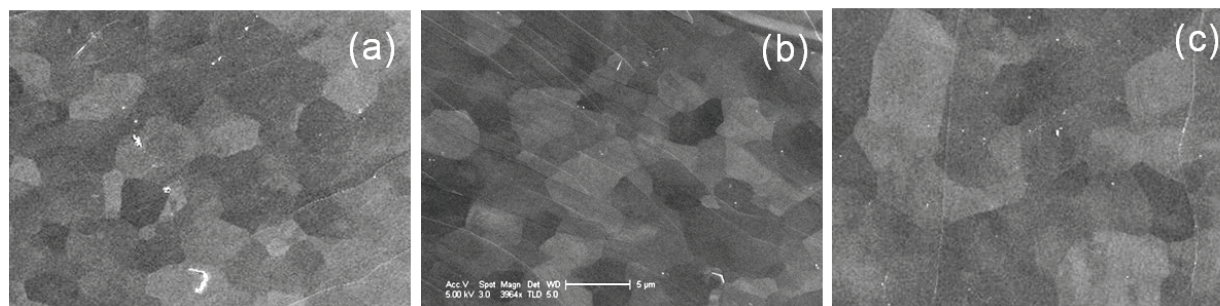


Figure S4. Typical, same-scale, SEM images of crystallites in different HOPG samples: (a) ZYH; (b) ZYA; (c) SPI. Typical crystallite sizes in ZYH, ZYB and ZYA are 2 to 5 μm ; in SPI crystallites vary from 0.5 to 15 μm . The scale bar corresponds to 5 μm .

To investigate whether the observed ferromagnetism is homogeneous within the same commercially available $1\text{cm} \times 1\text{cm} \times 0.2\text{cm}$ HOPG crystal, we measured magnetisation of four samples cut out from the same ZYH crystal as shown in the inset of Fig. S5. To exclude possible contamination of the samples due to exposure to ambient conditions, both exposed surfaces were cleaved and the edges cut off just before the measurements. Surprisingly, we found significant variations of the ferromagnetic signal between these four nominally identical samples – see Fig. S5.

This indicates that the observed ferromagnetism is not related to structural or other intrinsic characteristics of HOPG crystals, as these are the same for a given crystal. Therefore, it seems reasonable to associate the magnetic response with external factors, such as, for example, the presence of small inclusions of another material.

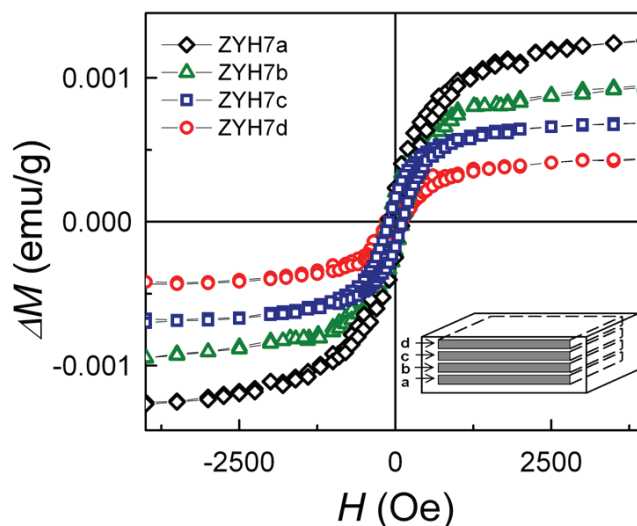


Figure S5. Ferromagnetic hysteresis in four samples cut from the same ZYH HOPG crystal. The inset shows schematically positions of the samples in the original crystal.

To check this hypothesis, we examined samples of different HOPG grades using backscattering SEM. Due to its sensitivity to the atomic number [S17], backscattered electrons can provide a strong contrast allowing to detect particles made of heavy elements inside a light matrix (graphite in our case). This experiment revealed that all ZYA, ZYB, and ZYH crystals contained sparsely distributed micron-sized particles of a large atomic number, with typical in-plane separations of 100 to 200 μm – see Fig. S6(a). Comparison of SEM images in backscattering and secondary electron modes (BS and SE, respectively) revealed that in most cases the particles were buried under the surface of the sample and, therefore, were not visible in the most commonly used secondary electron mode. This is illustrated in Fig. S6(b) which shows the same area of a ZYB sample in the SE and BS modes. The difference between the two images is due to different energies and penetration depths for secondary and backscattered electrons: The energy of BS electrons is close to the primary energy, i.e. ~ 20 keV in our case, and they probe up to $1\mu\text{m}$ thick layer at the surface [S17] while secondary electrons have characteristic energies of the order of 50 eV and come from a thin surface layer of a nm thickness [S18]. Importantly, no such inclusions could be detected in SPI samples that, as discussed, did not show any ferromagnetic response. The difference between ZY and SPI grades is presumably due to different manufacturing procedures used by different

suppliers. Our attempts through NT-MDT to find out the exact procedures used for production of ZY grades of HOPG were unsuccessful.

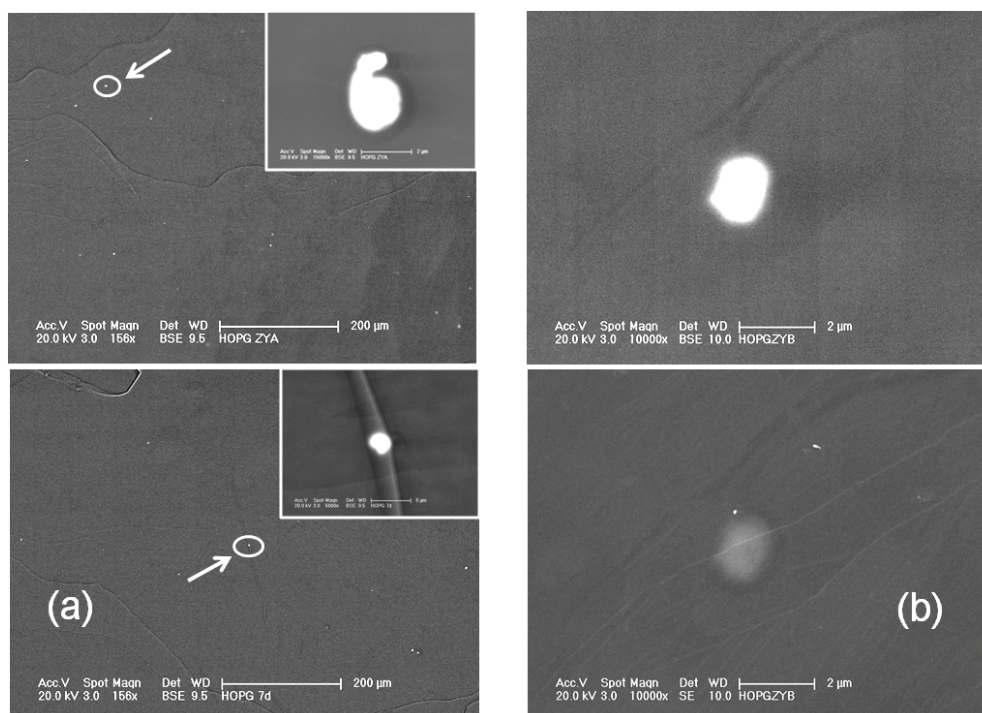


Figure S6. (a) SEM images of ZYA (top) and ZYH (bottom) samples in back-scattering mode. Small white particles are clearly visible in both images, with typical separations between the particles of 100 μm for ZYA and 240 μm for ZYH. Insets show zoomed-up images of the particles indicated by arrows; both particles are $\approx 2\mu\text{m}$ in diameter. (b) SEM images of the same particle found in a ZYB sample taken in backscattering (top) and secondary electron (bottom) modes. Surface features are clearly visible in the SE image while BS is mostly sensitive to chemical composition. The contrast around the particle in the SE mode is presumably due to a raised surface in this place.

To analyse the chemical composition of the detected particles we employed *in situ* energy-dispersive X-ray spectroscopy (EDX) that allows local chemical analysis within a few μm^3 volume. Figure S7 shows a typical EDX spectrum collected from a small volume (so-called interaction volume) around a 2.5 μm diameter particle in a ZYA sample. This particular spectrum corresponds to the presence of 8.6 wt% (2.1 at%) Fe, 2.3 wt% (0.65%) Ti, 1.8 wt% V (0.47 at%) and <0.5 wt% Ni, Cr and Co, as well as some oxygen, which appear on top of 86 wt% (96.5 at%) of carbon. The latter contribution is attributed to the surrounding graphite within the interaction volume. To determine the actual composition of the inclusion, we needed to take into account that the above elemental analysis applies to the whole interaction volume, where the primary electrons penetrate into the sample. Given that 96% of the interaction volume is made up by carbon, the electron range R and, accordingly, the interaction volume can be estimated to a good approximation using the Kanaya-Okayama formula [S19]:

$$R = \frac{0.0276 \cdot A \cdot E^{1.67}}{Z^{0.89} \cdot \rho} \approx 4.5 \mu\text{m},$$

where $A=12$ g/mole is the atomic weight of carbon, $E=20$ keV the beam energy, $Z=6$ the atomic number and $\rho=2.25$ g/cm³ the density of graphite. Using the calculated value of R , the weight percentages for different elements from the spectrum and their known densities, it is straightforward to show that the volume occupied by the detected amount of Fe and Ti is in excellent agreement with the dimensions of the particle in Fig. S7, i.e., the particle is made up predominantly of these two elements. The presence of oxygen indicates that Fe and Ti are likely to be in an oxidised state, i.e. the particle is either magnetite or possibly titanomagnetite, both of which are ferrimagnetic, with saturation magnetisation $M_S \approx 75\text{-}90\text{emu/g}$ [S20].

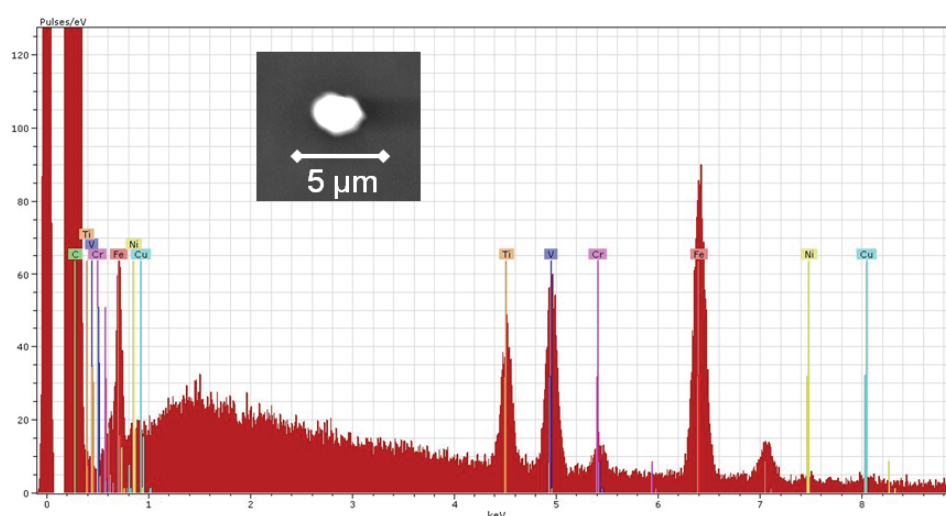


Figure S7. EDX spectrum of one of the particles found in a ZYA sample. Inset shows SEM image of the particle.

We estimate that a $2.5\mu\text{m}$ diameter particle of magnetite contributes $\approx 2.5 \cdot 10^{-9}$ emu to the overall magnetisation. Therefore, the observed ferromagnetic signal ($1.5 \cdot 10^{-5}$ emu) for this particular ZYA sample ($3 \times 3 \times 0.26$ mm) implies that the sample contains $\sim 6,000$ magnetite particles which, if uniformly distributed, should be spaced by $\sim 100 \mu\text{m}$ in the ab plane. This is in agreement with our SEM observations. This allows us to conclude that the visualized magnetic particles can indeed account for the whole ferromagnetic signal for this sample.

BS and EDX analysis of the other HOPG samples showing ferromagnetism produced similar results, with some samples containing predominantly Fe and others both Fe and Ti, as in the example above. A clear correlation has been found between the value of M_S for a particular sample and the average separation of the magnetic particles detected by BS/EDX – see Fig. S8. No

magnetic particles could be found in SPI samples and, accordingly, they did not show any ferromagnetic signal.

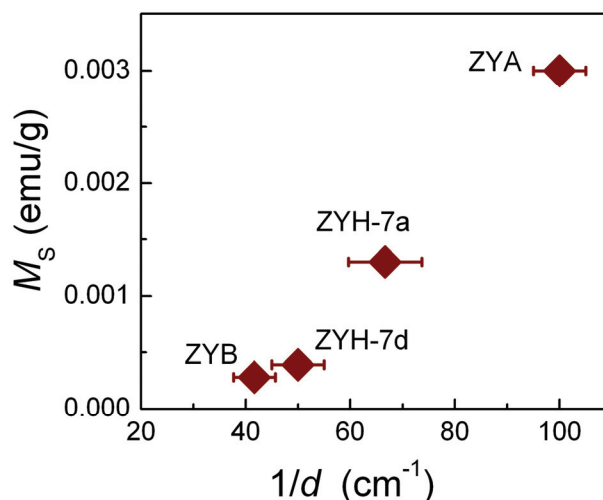


Figure S8. Saturation magnetisation M_s as a function of the inverse of the average separation between the detected particles d as determined from the backscattering images (see text).

On the basis of the above analysis, we conclude that ferromagnetism in our ZYA, ZYB and ZYH HOPG samples is not intrinsic but due to contamination with micron-sized particles of probably either magnetite or titanomagnetite. As these particles were usually detected at submicron distances below the sample surface (see above), they should have been introduced during high-temperature crystal growth. We note that ZYA, ZYB or ZYH grades of HOPG are most commonly used for studies of magnetism in graphite (e.g., ZYA-grade crystals were specified in refs. [S7, S9-S13]) and, therefore, the contamination could be the reason for the often reported ferromagnetism.

Finally, we would like to comment why magnetic particles such as those observed in the BS mode could have been overlooked by commonly used elemental analysis techniques, such as XRFS and PIXE [S7-S16]. Assuming that all particles found in our samples are magnetite and of approximately the same size, 2-3 μm , we estimate that the total number of Fe and Ti atoms in our samples ranges from 1 to 6 ppm. In the case of XRFS, 5 ppm of Fe is close to its typical detection limit and these concentrations might remain unnoticed. In the case of PIXE, its resolution is better than 1ppm. PIXE was used in e.g. refs. [S9, S11] for ZYA graphite, where no contamination was reported but the saturation magnetisation was $\approx (1-2) \cdot 10^{-3}$ emu/g, similar to our measurements. The absence of detectable concentrations of magnetic impurities has been used as an argument that the ferromagnetic signals could not be due to contamination. Also, it was usually assumed that any remnant magnetic impurities were distributed homogeneously, rather than as macroscopic particles,

and therefore would give rise to paramagnetism rather than a ferromagnetic signal, which was used as an extra argument against magnetic impurities.

It is clear that the latter assumption is incorrect, at least for the case of ZY grade graphite. Furthermore, let us note that the difference of several times for the limit put by PIXE and the amount measured by SQUID magnetometry is not massive. In our opinion, this difference can be explained by the fact that PIXE tends to underestimate the concentration of magnetic impurities if they are concentrated into relatively large particles. Indeed, PIXE probes only a thin surface layer ($\sim 1\mu\text{m}$ for 200 keV protons) which is thinner than the diameter of the observed magnetic inclusions. One can estimate that for round-shape inclusions with diameters of $\sim 3\mu\text{m}$, there should be a decrease by a factor of 3 in the PIXE signal with respect to the real concentration. Even more importantly, inclusions near the surface of HOPG provide weak mechanical points and are likely to be removed during cleavage when a fresh surface is prepared. Therefore, we believe that a micron-thick layer near the HOPG surface is unlikely to be representative of the whole sample. In contrast, magnetisation measurements probe average over the bulk of the samples, which can explain the observed several times discrepancy.

#5 Remnant ferromagnetism in graphene laminates

Preparation of graphene laminates involves splitting of graphite into individual graphene planes. Therefore, if standard HOPG ZYH or ZYA crystals are used, one can expect that magnetic particles present in the starting crystals may in principle pass into graphene laminates, despite the fact that centrifugation should mostly remove heavy particles from the suspension. Indeed, careful measurements of sufficiently large samples of graphene laminates made from ZYH-grade HOPG detected very weak ferromagnetic signals – see Fig. S9. For a typical 1.5-2mg graphene laminate sample the ferromagnetic component of magnetisation, M_S (300K), was found to be $< 5 \cdot 10^{-7}$ emu. Therefore, measuring the corresponding hysteresis loops required the maximum possible sensitivity of our SQUID magnetometer ($< 1 \cdot 10^{-7}$ emu), which we achieved by using the RSO option and taking great care in terms of sample mounting and background uniformity. Apart from the smaller M_S , all other characteristics of the ferromagnetic signal in the laminates (temperature independence, remnant magnetisation and coercive force) were similar to those for the starting HOPG samples, indicating the same origin of ferromagnetism – see Fig. S9.

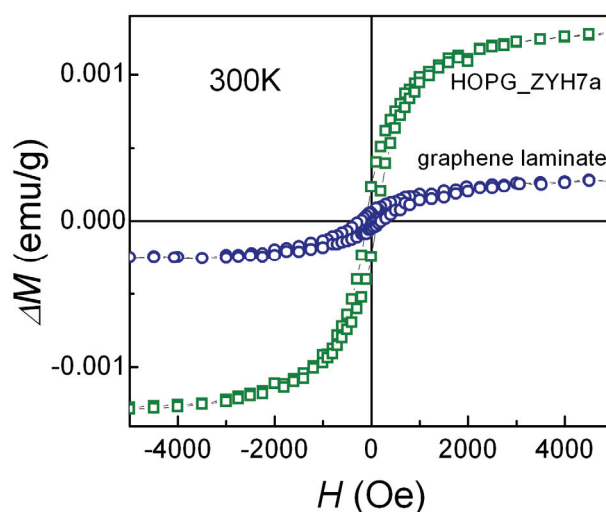


Figure S9. Comparison of the ferromagnetic magnetisation in HOPG ZYH and a typical sample of graphene laminate

Some samples used in our fluorination and irradiation experiments were additionally purified by immersion for several hours in a mixture of HNO_3 and HF acids and subsequent annealing at 300°C . The above acids are efficient in dissolving metal impurities, either in oxidised or pure metal form. After such treatment, no ferromagnetism was observed in any of these samples. Similar treatment of HOPG samples led to a reduction in M_S but not complete disappearance of the ferromagnetic signal. This result is easy to understand, as acids can penetrate between the decoupled graphene layers in laminate samples relatively easily, and this is not the case for bulk HOPG.

We conclude that the very weak but still detectable ferromagnetic response that we sometimes observed in graphene samples prepared from commonly available HOPG crystals also results from the initial contamination of HOPG, which should be taken into account when studying magnetic properties of graphene laminates and its derivatives.

Supplementary references

- S1. Nair, R. R. *et al.* Fluorographene: A two-dimensional counterpart of Teflon. *Small* **6**, 2877-2884 (2010).
- S2. Touhara, H., Okino F. Property control of carbon materials by fluorination. *Carbon* **38**, 241-267 (2000).
- S3. Robinson J. T. *et al.* Properties of fluorinated graphene films. *Nano Letters* **10**, 3001-3005 (2010).
- S4. <http://www.casaxps.com/>.
- S5. Telling R. H., Heggie M. I. Radiation defects in graphite. *Phil. Mag.* **87**, 4796-4846 (2007).

- S6. Gulans A., Krashennnikov A. V., Puska M. J., Nieminen R. M. Bound and free self-interstitial defects in graphite and bilayer graphene: A computational study. *Phys. Rev. B* **84**, 024114 (2011).
- S7. Esquinazi P., Setzer A., Höhne R., Semmelhack C. Ferromagnetism in oriented graphite samples. *Phys. Rev. B* **66**, 024429 (2002).
- S8. Cervenka J., Katsnelson M. I., Flipse C. F. J. Room-temperature ferromagnetism in graphite driven by two-dimensional networks of point defects. *Nature Physics* **5**, 840-844 (2009).
- S9. Esquinazi P. *et al.* Induced magnetic ordering by proton irradiation in graphite, *Phys. Rev. Lett.* **91**, 227201 (2003).
- S10. Quiquia B. *et al.* A comparison of the magnetic properties of proton- and iron-implanted graphite. *Eur. Phys. J. B* **61**, 127-130 (2008).
- S11. Makarova T. L., Shelankov A. L., Serenkov I. T., Sakharov V. I., Boukhvalov D. W. Anisotropic magnetism of graphite irradiated with medium-energy hydrogen and helium ions. *Phys. Rev. B* **83**, 085417 (2011).
- S12. He Z. *et al.* Raman study of correlation between defects and ferromagnetism in graphite. *J. Phys. D: Appl. Phys.* **44**, 085001 (2011).
- S13. Ramos M. A. *et al.* Magnetic properties of graphite irradiated with MeV ions. *Phys. Rev. B* **81**, 214404 (2010).
- S14. Talapatra S. *et al.* Irradiation-induced magnetism in carbon nanostructures. *Phys. Rev. Lett.* **95**, 097201 (2005).
- S15. Rode A. V. *et al.* Unconventional magnetism in all-carbon nanofoam. *Phys. Rev. B* **70**, 054407 (2004).
- S16. Ohldag H. *et al.* π -Electron ferromagnetism in metal-free carbon probed by soft X-ray dichroism. *Phys. Rev. Lett.* **98**, 187204 (2007).
- S17. Murata K. Exit angle dependence of penetration depth of backscattered electrons in the scanning electron microscope. *Phys. Stat. Sol. (a)* **36**, 197-208 (1976).
- S18. Eberhart J. P. *Structural and Chemical Analysis of Materials* (John Wiley & Sons, 1991)
- S19. Kanaya K., Okayama S. Penetration and energy-loss theory of electrons in solid targets. *J. Phys. D: Appl. Phys.* **5**, 43-58 (1972).
- S20. Goss C. J. Saturation magnetisation, coercivity and lattice parameter changes in the system Fe_3O_4 - $\gamma\text{Fe}_2\text{O}_3$, and their relationship to structure. *Phys. Chem. Minerals* **16**, 164-171(1988).